Dynamics of water evaporation from porous asphalt

M. Aboufoul [a*], N. Shokri [b], E. Saleh [c], C. Tuck [c], A. Garcia [a]

[a] *Nottingham Transportation Engineering Centre [NTEC], Department of Civil Engineering, University of Nottingham, Nottingham NG7 2RD, UK*

[b] *School of Chemical Engineering and Analytical Science, University of Manchester, Manchester, UK*

[c] *Centre for Additive Manufacturing (CfAM), University of Nottingham, Nottingham, NG7 2RD UK*

** Corresponding author. Tel: +44 (0) 0115 84 68437. E-mail address: mustafa.aboufoul@nottingham.ac.uk*

Abstract

The dynamics of water evaporation from porous asphalt mixture, with porosity ranging from 15% to 29%, have been investigated in this article. In order to test the same samples under different conditions, the pore structure of asphalt was quantified using X-ray Computed Tomography (CT) scans and 3D printed in transparent resin blocks. 3D printed transparent resin samples were tested under controlled laboratory conditions to understand the effect of pore space topology on the water retention and drying dynamics. The macroporosity, pore size distribution, air void tortuosity, water conductivity, and water retention curves of the 3D printed porous asphalt samples were quantified by means of image analysis. Moreover, a model was developed and tested experimentally to estimate the evaporation rates from porous asphalt materials under a wide range of porosities. Within the range of asphalt mixtures studied in the present work, the evaporation rate is related predominantly to the porosity, pore size distribution and tortuosity. It was found that the period over which water evaporation occurs at the surface is relatively short during drying of porous asphalt materials due to their relatively large pores weakening the capillary forces. This results in significantly shortening the so-called stage-1 evaporation (when the drying rate is controlled by liquid vaporisation at the surface) and early onset of the transition period (when both surface water evaporation and vapour diffusion inside porous asphalt play a comparable role in supplying the evaporative demand). The transition period is followed by the stage-2 evaporation when the process is limited by the vapour diffusion inside the porous asphalt. Our results illustrate that the beginning of the stage-2 evaporation depends on the porosity and tortuosity of the porous asphalt material among other parameters. Our results and analysis provide new insights into the dynamics of water evaporation from asphalt materials.

Keywords: water evaporation; porosity; asphalt mixture; X-ray CT; 3D printing.

1 INTRODUCTION

Evaporation from porous media plays a significant role in many industrial, environmental and engineering processes. These include water evaporation from land and building materials[1] including asphalt. Porous asphalt roads with porosity ranging from 15% to 29% have a complex pore structure network that can easily drain water [2]. For that reason, porous asphalt is often used to reduce runoff quantity and improve highway safety[3]. However, the internal pore structure of porous asphalt is exposed to water for long periods due to its high permeability [4], and moisture damage may happen, which may cause loss of the bond between the aggregate and binder surface and can result in stripping, cracking, and excessive permanent deformation [5]. The ability of the asphalt material to dry after exposure to water may affect its functionality and durability [6]. Therefore, in order to build durable roads, the evaporation process and the associated factors relevant to the evaporation in asphalt mixture need to be accurately investigated.

The main two factors affecting the evaporation rate from porous media filled with water are (i) atmospheric conditions such as temperature, humidity and air velocity and (ii) the topology of pore spaces and their transport properties which affects hydraulic conductivity and vapour diffusion [7]. Typically, evaporation from porous media comprises two stages. During stage-1, the evaporation rate is rather high and the surface of porous media remains partially wet caused by the capillary-induced liquid flow supplying water from the receding drying front (defined as the interface between saturated and partially wet zone) to the evaporation surface. Disruption of capillary liquid pathways (due to the interplay between capillary, gravity and viscous forces) marks the onset of stage-2 evaporation characterised by a much lower evaporation rate which is limited by the vapour diffusion through the porous medium [8].

Jerjen et al. [9] applied X-ray micro-Computed Tomography (CT) to investigate the drying of porous asphalt. They found that the drying process depends on topological properties of the porous asphalts such as mean pore volume, diameter and the pore network structure. Poulikakos et al. [10] studied the drying of porous material in the presence of wind following a severe rain event, when the entire pore volume of the porous structure was fully saturated with water. They found a relatively fast evaporation rate at the beginning of the process followed by much lower evaporative fluxes as a result of the disconnection of liquid pathways. Lal et al. [11] found that even after the porous asphalt had been allowed to dry for an extended period of time, it still had residual water inside influenced by the complex porous structure. The above references suggest that understanding the effect of pore structure on the dynamics of liquid transport and distribution during evaporation is of extreme importance for designing porous asphalt materials that are less water sensitive.

3D printing has demonstrated great potential for studying flow and transport processes in porous media due to the unprecedented freedom of design offered by this technique [12-15]. The concept of using 3D printing to replicate complex porosity in rocks has been reported by Head et al. and Ishutov et al. [16, 17]. These studies showed the feasibility of combining CT images with 3D printing technology to fabricate a porous

material with similar structure to the real porous sample. This provides us with a unique opportunity to fabricate porous asphalt using 3D printing technology for investigation of the water evaporation process.

Motivated by the importance of understanding the interaction between porous asphalt and water and its influences on asphalt durability, the specific objectives of this investigation are to understand the dynamics of water evaporation in porous asphalt material. To do this, we have quantified the dynamics of water distribution during evaporation in porous asphalt, by conducting evaporation experiments using 3D printed transparent resin blocks with structure equivalent to asphalt, captured from X-ray computed tomography scans of real asphalt samples with porosity ranging from 15% to 29%. Furthermore, CT scan results have been used to assess the air void structure of asphalt test samples. This enabled us to investigate the relationship between the pore space topological properties and the water evaporation dynamics of the asphalt mixture. Finally, a model was proposed to describe the drying curves measured during evaporation from porous asphalt samples investigated in this study.

2 MATERIALS AND METHODS

2.1 Porous asphalt samples description

Four asphalt slabs of approximately 300 mm x 300 mm x 50 mm were manufactured with bitumen 60/40 penetration grade and crushed limestone aggregates of 20 mm maximum size. These mixtures aimed to represent commonly used porous asphaltic materials in roads (see Table 1 for the aggregate gradation and binder content used in the mixtures). Aggregates and bitumen were mixed at 160 °C and roller-compacted at 140 °C to reach the target porosity of 13%, 17%, 21%, and 26%, following the standard BS EN 12697-33[18]. Finally, two cores of 100 mm diameter and 50 mm height were extracted from each slab and their internal air void structure was quantified using X-ray Computed Tomography scans.

2.2 X-ray Computed Tomography (CT) scans of asphalt mixture

Asphalt cores were scanned under dry condition using a Phoenix v|tome|x L 300 micro CT scanner; the X-ray tube used is (MXR320HP/11, 3.0mm Be +2mm Al from GE Sensing and Inspection Technology) and was operated with an acceleration voltage of 290 kV and a current of 1300 µA.

The X-ray CT scans were carried out in the micro computed tomography Hounsfield facility at the University of Nottingham. The samples were mounted on a rotational table at a distance of 906.84 mm from the X-ray source. The reconstruction of scans was performed on GE Datos|x reconstruction software with 2x resolution to obtain a spatial resolution of 45.2 µm; the scans had an isotropic resolution, meaning that the slice thickness was also 45.2 µm.

The images were originally 16-bit (.tiff format) and the voxel value represented the x-ray attenuation. The images were processed with the software tools Avizo 8.1 and ImageJ, Version 1.49 [19], the images were converted to 8-bit grayscale resolution. 3D Gaussian and Median filters (1 x 1 x 1 Kernel size) were used to reduce the noise in the images.

Reconstructions of the microstructure were prepared by segmenting the materials based on grayscale thresholding using ImageJ. This allows separating aggregates, bitumen and air voids. Since small isolated clusters of voids or grain voxels may correspond to small isolated pores or to noise effects [20], these were removed from the image prior further analyses. Therefore, all features less than 0.5 mm in diameter were removed from the binary segmented data to prevent being classified as pores. The segmented images of the air voids were stacked in Avizo 8.1 generating 3D surfaces that encase each group of neighbouring pixels belonging to a common void space.

2.3 3D printing material and technology

Stereolithography (SLA) printing was used to reproduce asphalt mixture due to the vast capabilities of the technology to produce fine channels and pores with high resolution (25 to 100 µm)[17]. Common materials used in SLA are acrylic clear or translucent resins that contain photo-initiators. When the resin is irradiated with a laser of a wavelength that matches its photo-initiator, a rapid solidification occurs in the form of photo-polymerisation. The 3D printing process was arranged by scanning the surface of the resin with a laser beam to match the required shape, layer by layer, to form a complete 3D structure. The printed structure was then submerged in isopropanol alcohol (IPA) for 5 minutes to make sure all resin within the pores had come out. Moreover, the average water wetting contact angle of the samples made with SLA printing materials is 68.7°±7.67 [21] suggesting that the printing materials used in SLA technology can simulate asphalt mixture with relatively similar wetting characteristics since the mean water wetting contact angle of bitumen 60/40 penetration grade is 93.04°[22], and the approximate water wetting contact angle of limestone is 59.0°[23]. The wetting contact angle of mastic is between these two values, which is in the range of SLA printing materials.

Furthermore, it is important to note that using the SLA printer with a resolution of 50 µm to 3D print digital models of porous asphalt materials will neglect the very fine parts of the pore structure; such as pores with diameter < 50 µm.

2.4 Preparation of 3D printed asphalt samples

Firstly, the pore structure of asphalt materials was quantified using X-ray CT scans to generate 3D models of different porosity, as explained in section 2.2.

Secondly, digital Regions of Interest (RoI) of 80 mm x 25 mm x 40 mm were obtained from the centre of the 3D models. The sample dimensions were considered representative of asphalt, as the dimensions should be between 2.5 to 3 times the maximum aggregate size, as has been stated in [24].

Thirdly, 3D models were fabricated using a Formlabs Form 2 printer with 50 μm resolution. Commercially available Formlabs Clear FLGPCL02 proprietary resin [25] was used to produce the transparent plastic model. Finally, the support structure was cut manually from the model and then submerged in isopropanol alcohol for 10 minutes, to make sure that all the resin within the pores had been removed. Finally, the samples were polished using super fine 600-grit sandpaper and finished with acrylic spray to enhance samples transparency [26]. (See Figure 1 (a) for a typical sample of the 3D printed block with the pore structure of an asphalt test sample).

2.5 Water evaporation experimental set up

The water evaporation experimental set-up and arrangement of instruments are shown in Figure 1(b). A transparent and waterproof container made of 5 mm thick acrylic plastic with internal dimensions of 80 x 25 x 50 mm^3 was used to hold the 3D printed asphalt sample from all sides except the top which was open for evaporation. The sample was placed on a digital balance Ohaus ranger 3000, with accuracy 0.05g, to record the mass loss during evaporation at 5 min intervals. During the experiment, the sample was placed in a fully insulated temperature control chamber at 40 ± 2℃ (Incubator TC 135S, Lovibond) and the relative humidity inside the chamber was 10 ± 2% monitored using hygrometer sensor (Oregon Scientific BAR206).

A full HD digital camera AW920 (AUSDOM) was used to monitor the displacement of the drying front (defined as the interface between saturated and partially saturated zones) inside the porous asphalt during evaporation with a temporal resolution of 5 min. A blue coloured water with 5% of colourant concentration was used to enhance the contrast between saturated and partially wet zones.

Evaporation from the asphalt mixture was investigated under saturated and semi-saturated conditions to simulate field conditions as well as to give an overview on evaporation dynamics from fully saturated to fully dry condition. Under saturated conditions, the 3D printed specimen was placed in the test container, and the 3D printed specimen was filled with coloured water until it was fully saturated, and water covered its surface before the evaporation test started. Under semi-saturated conditions, the 3D printed specimens were first saturated with coloured water and then, the water was allowed to drain from the bottom of the specimens. This allowed the simulation of water contained in asphalt after a rain event. In this test, the sides of the 3D printed specimens were wrapped with a transparent film to avoid moisture losses, while the top and bottom sides were open to air, to allow water drainage from the bottom. When most of the water drainage was completed, the bottom side of the 3D printed specimen was closed and sealed before the evaporation test started.

2.6 Topology of air voids

The macropore characteristics of 3D printed blocks including macroporosity, average void diameter, pore-size distribution, and tortuosity were quantified using X-ray CT scans. These are commonly used properties to analyse the topology of porous media [27]. The macroporosity was calculated as the volume of macropores per unit of volume in the RoI. The average void diameter was calculated using a thickness algorithm within the Particle Analyser plugin in ImageJ [19]. The pore-size distribution was calculated using a thickness algorithm within the ImageJ plugin called BoneJ, as defined in reference [28].

The tortuosity was calculated from tomographic X-ray data as the ratio between the total macropore length and the total shortest distance between the ends of all macropores [29]. Macropore tortuosity was obtained using a 3D morphological (iMorph) software package [30].

In addition, we quantified the so-called Water Retention Curve (WRC) of the asphalt sample used in our experiments. The WRC determines the relationship between the capillary head and water saturation of the asphalt sample. The WRC is an important hydraulic property related to the size and conductivity of the pore space which is used to describe liquid flow in porous media [31]. To calculate it, the cumulative pore-size distribution curve was first divided into a number of classes (n) representing the different pore size ranges, with an interval of 0.25 mm among them. Once the pore radius (r_i) was found for the upper limit of each class n, the corresponding asphalt capillarity head (h_i) could be calculated for each class according to the following equation [32]:

$$h_i = \frac{2\gamma cos\theta}{\rho_w g r_i} \quad (1)$$

where γ is water surface tension (N/m), θ is the contact angle of 3D printed materials (68.7°[21]), ρ_w is the density of water (kg/m^3), g is the gravitational acceleration (m/s^2), and r_i is the pore radius (m).

3 RESULTS AND DISCUSSION

3.1 Pore space topological properties and pore size distribution of porous asphalts

Figure 2 (a) shows the cumulative pore size distribution of the asphalt samples with porosity ranging from 15% to 29%. Table 2 shows that the samples with higher porosity have a larger pore diameter, as the average pore diameter increases from 1.7 mm to 2.5 mm when porosity changes from 15% to 29%. It must be noted that in our porous asphalt materials, we observed a significant number of macropores with diameter of 3 mm to 6 mm. These macropores play a key role in water drainage and the evaporation behaviour of porous asphalt materials [33].

The relationship between the capillary pressure and water content in 3D printed transparent resin blocks was determined using a pore size distribution approach as mentioned in section 2.5. The resulting water retention curve for the test sample with 15.6% porosity (AVC) is presented in Figure 2 (b) as an example. Moreover, Figure 2 (b) shows the method used to estimate the evaporation characteristic length L_c (defined as the maximum length of the capillary liquid pathways sustaining water flow from the saturated zone to the surface of the porous asphalt) following the procedure introduced in reference [7]. To do so, the tangent line is drawn at the inflection point of the curve and L_c is calculated by the difference of the capillary head values where the tangent line intersects with water saturation values of 0% and 100%. The results show that L_c decreases with increasing porosity in our samples. In particular, L_c decreases from 1.7 mm for test samples with 15.6% AVC to less than 1 mm for test samples with 29.8% AVC, see Table 2. This is expected because, as mentioned above, in our samples a higher porosity corresponds to larger pore sizes leading to sharper WRC hence shorter L_c.

3.2 *Dynamics of water evaporation from saturated porous asphalt*

Figure 3 (a) shows the measured cumulative water mass loss during evaporation from the asphalt mixture with porosity ranging from 15% to 29%. The gradients of the cumulative mass loss with time curves correspond to the rate of evaporation [7].

The duration of stage-1 evaporation, t_c, and the start of stage-2 evaporation, $t_{2,}$ were estimated following the procedure used in [34]. The length of stage-1 was calculated, based on the change in slope of the total cumulative mass loss curve over time, as the moment when the curve diverted from a tangent straight line drawn from the start of the drying experiment, see Figure 3(a). The length of the stage-1 evaporation period decreases with porosity, for example, from 315 min to 230 min for asphalt samples with a porosity of 29% and 15%, respectively. From L_c data shown in Table 2, it can be concluded that stage-1 evaporation in the porous asphalts investigated in our experiments is negligible when compared to the total duration of the drying process, which is in the range of days. This is because of the relatively large pores of the asphalt samples used in our experiments. This reduces the capillary forces hence shortening the duration of stage-1 evaporation. Stage-1 evaporation is followed by the transition period. Results in Figure 3(a) show that test samples with lower porosity, such as 15% and 16%, have a sharp transition period to stage-2 of evaporation, whilst test samples with porosity above 17%, have a more gradual transition periods before the onset of stage-2, due to their more connected and open pore structure which influences the dynamics of the transition period [2].

3.3 Drying front displacement during evaporation from saturated porous asphalt

The change in the drying front depth measured during evaporation from the asphalt samples is shown in Figure 4. To measure it, the images captured during the evaporation test were cropped to the exact size of the test samples and then segmented into binary images where black pixels represent pores that are fully

saturated with water. The length measurement tool in ImageJ software was used to measure the distance from the surface of the sample to the water level (see Figure 4 inset). Results suggest that the drying front's recession rate reduced with time. This happens because of the gradual loss of the hydraulic connections between the drying front and the surface during the transition stage. For example, in asphalt with 29.8% porosity it takes 1200 min to dry the first 15 mm and 4600 min to dry the next 15 mm. In addition, the recession rate of the evaporation front is smaller in test samples with higher porosity. For example, the evaporation front in asphalt with 29.8% porosity needs approximately 5800 minutes to reach a depth of 30 mm, while it needs 2880 min for the asphalt mixture with 17.9% porosity.

3.4 Water evaporation dynamics of partially-saturated porous asphalt

Figure 5 shows the cumulative evaporative water losses measured during evaporation from four partially-saturated 3D printed blocks, with porosity ranging from 16% to 29%. The graph shows that the sample with a higher porosity, 29.8%, has a shorter transition period as stage-2 began 360 min after the start of the test, while the sample with a lower porosity, 17.9%, shows a much longer and gradual transition period before the onset of stage-2, taking about 600 min. At the start of the experiment, a steeper slope indicates that there is a sharp drop in the drying rate, this period is mainly controlled by the amount of residual water accumulated in the pores near the surface, which depends on void structure. Also, the duration of stage-1 evaporation is negligible here due to the relatively large pores of the porous asphalt material which result in weak capillary forces.

Moreover, it can be seen in Figure 5 that the transition period is longer for the sample with 17.9% porosity, compared to the sample with 29.8% porosity, unlike the results in the full saturation case. This might be due to the presence of more trapped water near the surface, as can be seen in the inset of Figure 5, compared to the sample with higher porosity where almost all the water is found at the bottom of the sample.

Once the surface starts to dry, the number of capillary pathways connecting the drying front to the surface reduces which results in the reducing evaporation rate. When the surface is fully dried, it marks the onset of stage-2 evaporation. Drying rate in this stage is controlled by the water vapour diffusion in the porous material, which depends on the porosity and tortuosity of the network (among other parameters). The sample with 29.8% porosity has higher stage-2 evaporation rates, ranging from 0.001 g/min to 0.0005 g/min, while the sample with 17.9% porosity has lower stage-2 evaporation rates ranging from 0.0008 g/min to 0.00028 g/min. This is possibly due to the fact that the sample with 29.8% porosity has more continuous air void connection and less tortuosity, as shown in Table 2, which contribute to the diffusive evaporative water fluxes during stage-2 evaporation. Another reason could be related to the thickness of the dry region formed close to the surface at the onset of stage-2 which is a function of pore size (among other parameters). This thickness influences the diffusion length thus the magnitude of the evaporation rate [8].

3.5 Estimation of the water evaporation rate from porous asphalt.

As it was mentioned earlier, the duration of stage-1 evaporation is negligible during evaporation from porous asphalt samples investigated in the present study because of the presence of relatively large pores in the porous media which weakens the capillary forces. Consequently, one may conclude that the evaporation process from porous asphalt mainly includes the transition period and the stage-2 evaporation (when the surface is fully dried). In the following, a theoretical framework is developed to describe the measured fluxes during evaporation from asphalt samples.

Pure water evaporation (e_D) takes place by vapour diffusion through thin layers of air above the asphalt (δ), due to the concentration gradient between fully saturated vapour at the surface of the asphalt and the air vapour concentration above the asphalt surface [35]. Pure water evaporation (e_D) from the surface depends on the atmospheric boundary conditions and the evaporation surface (A) among other parameters [36, 37] and can be estimated using Fick's law as:

$$e_D = A \cdot D \cdot \frac{C_{sat} - C_\infty}{\delta} \quad (2)$$

where D is the vapour diffusion coefficient in free air (0.00166 m^2/min [38]), C_{sat} is the saturated water vapour density, and C_∞ is the water vapour density above the surface (g/m^3).

On the other hand, to calculate the evaporation rate at the stage-2 evaporation, it is required to know the distance from the sample surface to the boundary between the dry and the partially-saturated regions, or the diffusion length (ζ). In this research, this value was estimated by monitoring the depth of the drying front inside the transparent printed samples which was used to calculate the evaporation rate during the stage-2 evaporation from a modified version of Fick's law [39]:

$$e_{II}{}^*(\mathrm{t}) = D^{eff} \cdot \frac{C_{sat} - C_\infty}{\zeta} \quad (3)$$

where $e_{II}{}^*(\mathrm{t})$ is the rate of evaporation during stage-2 (g/min), D^{eff} is the effective vapour diffusion coefficient in porous media (m^2/min), calculated using $D^{eff} = D\frac{\varepsilon}{\tau}$ [40], τ is the tortuosity factor, ε is the porosity, obtained from Table 2, C_{sat} is the saturated water vapour density (51 g/m^3 [38]), C_∞ is the water vapour density above the surface (g/m^3), $and\ \zeta$ is the vapour diffusion length which increases with time (m).

The dynamics of the evaporation process during the transition period depend on the topological properties of the asphalt material (e.g. pore size distribution and shape), the ambient humidity and temperature [39]. To

model the evaporation rate in asphalt material, we hypothesise that the evaporation rate during the transition stage (e_t) can be estimated as a combination of e_D and e_{II}, as shown in Figure 6.

At the start of the transition stage (t_1), the water in the pores at the upper surface regions of the material diffuses directly into the atmosphere at the rate of e_D. When the drying front begins to recede inside the material, the water in the small pores at the surface layers will continue evaporating directly into the atmosphere. As a consequence of the pure water evaporation, the total area of the pores that are directly connected to the surface (A) decreases. For this reason, e_D during the transition period will be a function of time and decrease until it reaches zero. At the same time, water pockets start to appear that are cut from the top layers of the material and moisture in these pores has to diffuse through the material at the rate of e_{II}. The cumulative contribution of this mechanism towards supplying the evaporative demand increases over time until most of the connections of the water inside the pores to the surface are lost and e_{II} is predominant. When all liquid pathways are disconnected, this marks the onset of stage-2.

Therefore, the evaporation rate during the transition period (e_t) could be described as the sum of the direct evaporation, e_D, and the diffusive evaporation, e_{II}:

$$e_t(t) = e_D(t) + e_{II}(t) \tag{4}$$

Note that the cumulative contribution of e_D, and e_{II}, towards the total evaporative mass losses decreases, and increases, respectively during the transtion period (see Figure 6). Furthermore, we know that $e_t(t_1) = e_D(t_1)$ and $e_t(t_2) = e_{II}(t_2)$, where $t_1$and t_2 correspond to the onset and the end of transition period.

To develop an analytical tool capable of describing the measured evaporative fluxes during the transition period in our experiments, we hypothesise that A decreases with time in a logarithmic way (based on the results shown in Figure 4, which show a logarithmic evolution of the evaporation front with time). Thus $A(t) = -X\ln(t) + Y$, where X and Y are the fitting parameters depending on the speed of the receding drying front. In addition, when $t = t_2$, $A(t) = 0$ m^2, one could conclude that $t_2 = e^{\frac{Y}{X}}$. As the area A, changes with time, Eq. (3) can be re-written as:

$$e_D(t) = D \cdot \frac{C_{sat} - C_\infty}{\delta} \cdot A(t) \tag{5}$$

The second process affecting the transition period is the diffusive evaporation (e_{II}) through the sample in the transition region. At the start of the transition period, $A(t_1)$ is assumed to be 0 m^2, and increases following a logarithmic trend until it reaches $A(t_2)$, which corresponds to the highest value of the evaporation due to the diffusion at the start of the stage-2, Figure 6. Therefore, one could write:

$$e_{II}(t) = e_{II}{}^{*}(\mathrm{t}) \cdot \left(1 - \frac{A(t)}{A(t_1)}\right) \quad (6)$$

By substituting Eqs. 5 and 6 in Eq.4, the evaporation rate during the transition period can be expressed as:

$$e_t(t) = \left(D \cdot \frac{C_{sat} - C_{\infty}}{\delta} \cdot (-X \ln(t) + Y)\right) + e_{II}(\mathrm{t}) \cdot \left(1 - \frac{(-X \ln(t) + Y)}{(-X \ln(t_1) + Y))}\right) \quad (7)$$

where X and Y are the fitting parameters depending on the topology of the asphalt material and are related to the starting time of the stage-2 evaporation t_2. We have fitted equations (3) and (7) on the measured experimental data during the evaporation process from fully and partially saturated 3D printed blocks with 17.9% and 29.8% porosity. The results are presented in Figure 7 (a,b). The comparison between the values predicted by the model and the experimental data suggests a reasonable performance of the proposed model in describing the evaporation process from porous asphalts.

4 CONCLUSIONS

In this paper, the evaporation dynamics from porous asphalt materials have been investigated experimentally and theoretically. We have fabricated 3D porous asphalt with state-of-the-art 3D printing technology. The design of the porous asphalt was based on the structure of real asphalt imaged by X-ray micro-tomography. Different 3D printed porous asphalts, varying in their porosity, were used to study the dynamics of water evaporation. In particular, the following conclusions have been drawn:

1- Evaporation in asphalt mixture may happen directly into the atmosphere controlled by surface evaporation or through moisture evaporation inside the porous asphalt followed by vapour diffusion through the medium. The effect of the topology of air void structure plays a key role on the evaporative fluxes because increasing the porosity, pore size and connectivity will influence the liquid and vapour transport through the porous asphalt which eventually influences the evaporation behaviour.

2- The so-called stage-1 evaporation (the period when the drying process is controlled by the external conditions) was relatively short during evaporation from the porous asphalt samples used in the present study. This is because of the relatively large pores of the 3D printed porous asphalt which weakened the capillary forces thus shortening the period over which the receding drying front is hydraulically connected to the surface which is required to sustain the stage-1 evaporation. However, both the transition period (when both surface water evaporation and vapour diffusion through porous

asphalt are important in supplying the evaporation demand) and the stage-2 evaporation (when the drying process is controlled by vapour diffusion through the porous asphalt) were observed during drying of the porous asphalt samples investigated in the present study.

3- We proposed an empirical model taking into account the contribution of surface water evaporation as well as vapour diffusion through the porous asphalt to describe the measured evaporative mass losses from the porous asphalt samples. The effects of porosity and tortuosity of porous asphalt material were taken into account in the proposed empirical equation.

4- As a general conclusion, our study illustrates the great potential of 3D printing technology to study the dynamics of water evaporation from asphalt material and provides a high level of detail that is comparable to X-ray and neutron computed tomography techniques. In the future, the evaporation model proposed in this research and 3D printing technology can be extended to a wider range of road topologies, such as those composed of layers with different porosity, to accelerate or reduce the evaporation rate of asphalt roads depending on the topology of the asphalt air void structure. Finally, the influence of wind and environmental conditions on the dynamics of evaporation from asphalt mixture needs to be studied in detail.

ACKNOWLEDGEMENTS

The authors would like to acknowledge the University of Nottingham, United Kingdom which has funded this research through the Dean of Engineering Research Scholarship for International Excellence. Nima Shokri acknowledges funding by Royal Academy of Engineering-The Leverhulme Trust Senior Research Fellowship (LTSRF1718\14\8).

REFERENCES

1. Shahraeeni, E. and D. Or, *Pore-scale analysis of evaporation and condensation dynamics in porous media.* Langmuir, 2010. **26**(17): p. 13924-13936.
2. Aboufoul, M. and A. Garcia, *Factors affecting hydraulic conductivity of asphalt mixture.* Materials and Structures, 2017. **50**(2): p. 116.
3. Scholz, M. and P. Grabowiecki, *Review of permeable pavement systems.* Building and Environment, 2007. **42**(11): p. 3830-3836.
4. Aboufoul, M. and A. Garcia, *Influence of air voids characteristics on the hydraulic conductivity of asphalt mixture.* Road Materials and Pavement Design, 2017: p. 1-11.
5. Kassem, E., et al., *Measurements of the moisture diffusion coefficient of asphalt mixtures and its relationship to mixture composition.* International Journal of Pavement Engineering, 2009. **10**(6): p. 389-399.
6. Poulikakos, L., et al., *Time resolved analysis of water drainage in porous asphalt concrete using neutron radiography.* Applied Radiation and Isotopes, 2013. **77**: p. 5-13.
7. Lehmann, P., S. Assouline, and D. Or, *Characteristic lengths affecting evaporative drying of porous media.* Physical Review E, 2008. **77**(5): p. 056309.
8. Shokri, N. and D. Or, *What determines drying rates at the onset of diffusion controlled stage-2 evaporation from porous media?* Water Resources Research, 2011. **47**(9).
9. Jerjen, I., et al., *Drying of Porous Asphalt Concrete Investigated by X-Ray Computed Tomography.* Physics Procedia, 2015. **69**: p. 451-456.
10. Poulikakos, L.D., et al., *Forced convective drying of wet porous asphalt imaged with neutron radiography.* Advanced Engineering Materials, 2013. **15**(11): p. 1136-1145.
11. Lal, S., et al., *Wetting and drying in hydrophobic, macroporous asphalt structures.* Construction and Building Materials, 2017. **152**: p. 82-95.
12. MacDonald, E. and R. Wicker, *Multiprocess 3D printing for increasing component functionality.* Science, 2016. **353**(6307): p. aaf2093.
13. Goodridge, R., C. Tuck, and R. Hague, *Laser sintering of polyamides and other polymers.* Progress in Materials Science, 2012. **57**(2): p. 229-267.
14. Saleh, E., et al., *3D inkjet printing of electronics using UV conversion.* Advanced Materials Technologies, 2017. **2**(10).
15. Osei-Bonsu, K., P. Grassia, and N. Shokri, *Relationship between bulk foam stability, surfactant formulation and oil displacement efficiency in porous media.* Fuel, 2017. **203**: p. 403-410.
16. Head, D. and T. Vanorio, *Effects of changes in rock microstructures on permeability: 3-D printing investigation.* Geophysical Research Letters, 2016. **43**(14): p. 7494-7502.
17. Ishutov, S., et al., *Using Resin-Based 3D Printing to Build Geometrically Accurate Proxies of Porous Sedimentary Rocks.* Groundwater, 2017.
18. BS EN 12697-33, B.S.I.B., Bituminous Mixtures, Test Methods for Hot Mix Asphalt: Specimen prepared by roller compactor, 2003.
19. Abràmoff, M.D., P.J. Magalhães, and S.J. Ram, *Image processing with ImageJ.* Biophotonics international, 2004. **11**(7): p. 36-42.
20. Peth, S., et al., *Three-dimensional quantification of intra-aggregate pore-space features using synchrotron-radiation-based microtomography.* Soil Science Society of America Journal, 2008. **72**(4): p. 897-907.
21. Bacher, M., *3D-printing of undisturbed soil imaged by X-ray.* 2013.
22. Ahmad, N., *Asphalt mixture moisture sensitivity evaluation using surface energy parameters*. 2011, University of Nottingham.

23. Wei, J. and Y. Zhang, *Application of sessile drop method to determine surface free energy of asphalt and aggregate*. Journal of Testing and Evaluation, 2012. **40**(5): p. 807-813.
24. Lal, S., et al., *Investigation of Gravity-Driven Drainage and Forced Convective Drying in a Macroporous Medium Using Neutron Radiography*. Transport in Porous Media, 2017: p. 1-24.
25. Okafor, O., et al., *Advanced reactor engineering with 3D printing for the continuous-flow synthesis of silver nanoparticles*. Reaction Chemistry & Engineering, 2017. **2**(2): p. 129-136.
26. Yoon, H., M.J. Martinez, and T. Dewers, *3D Printing and Digital Rock Physics for Geoscience Applications*. 2016, Sandia National Lab.(SNL-NM), Albuquerque, NM (United States).
27. Katuwal, S., et al., *Effects of CT number derived matrix density on preferential flow and transport in a macroporous agricultural soil*. Vadose Zone Journal, 2015. **14**(7).
28. Doube, M., et al., *BoneJ: free and extensible bone image analysis in ImageJ*. Bone, 2010. **47**(6): p. 1076-1079.
29. Pardo-Alonso, S., et al., *Geometrical tortuosity 3D calculations in infiltrated aluminium cellular materials*. Procedia Materials Science, 2014. **4**: p. 145-150.
30. Vicente, J., Y. Wyart, and P. Moulin, *Characterization (2D-3D) of ceramic microfiltration membrane by synchrotron radiation: new and abraded membranes*. Journal of Porous Media, 2013. **16**(6): p. 537-545.
31. Hines, J., C.S. John, and E. Pease, *Hydraulic properties of asphalt concrete*. 2010.
32. Dong, X. and B. Patton, *Predicting soil water retention curves based on particle-size distribution using a Minitab macro*. Afr J Soil Sci, 2015. **3**(1): p. 079-085.
33. Lal, S., *Multiscale investigation and numerical modeling of imbibition, drainage and drying of a macroporous medium*. 2016.
34. Saadoon, T., A. Garcia, and B. Gómez-Meijide, *Dynamics of water evaporation in cold asphalt mixtures*. Materials & Design, 2017. **134**: p. 196-206.
35. Or, D., et al., *Advances in soil evaporation physics—A review*. Vadose Zone Journal, 2013. **12**(4).
36. Vanderborght, J., et al., *Heat and water transport in soils and across the soil-atmosphere interface: 1. Theory and different model concepts*. Water Resources Research, 2017. **53**(2): p. 1057-1079.
37. Shokri-Kuehni, S.M., et al., *Impact of type of salt and ambient conditions on saline water evaporation from porous media*. Advances in water resources, 2017. **105**: p. 154-161.
38. Cussler, E.L., *Diffusion: mass transfer in fluid systems*. 2009: Cambridge university press.
39. Shokri, N., P. Lehmann, and D. Or, *Critical evaluation of enhancement factors for vapor transport through unsaturated porous media*. Water resources research, 2009. **45**(10).
40. Cooper, S., et al., *TauFactor: An open-source application for calculating tortuosity factors from tomographic data*. SoftwareX, 2016.

TABLES

Table 1: Aggregate grading and binder content used to produce asphalt mixtures.

Target porosity	13%	17%	21%	26%
sieve size (mm)	Cumulative aggregate weight % passing			
63.000	100.0	100.0	100.0	100.0
40.000	100.0	100.0	100.0	100.0
31.500	100.0	100.0	100.0	100.0
20.000	99.0	99.0	100.0	99.0
16.000	91.0	91.0	96.0	91.0
14.000	83.0	82.0	88.0	78.0
10.000	56.0	51.0	53.0	28.0
8.000	44.0	39.0	36.0	18.0
6.300	34.0	29.0	23.0	14.0
4.000	25.0	21.0	18.0	11.0
2.800	21.0	19.0	17.0	10.0
2.000	18.0	16.0	14.0	9.0
1.000	13.0	11.0	10.0	7.0
0.500	10.0	9.0	8.0	5.0
0.250	8.0	7.0	6.0	4.0
0.125	6.0	6.0	5.0	4.0
0.063	5.0	5.0	4.0	3.0
Binder content (%)	4.2	3.8	3.3	3.2

Table 2: Topological constants of 3D printed transparent resin blocks.

Sample No.	Macroporosity	Average void diameter	Maximum void diameter	Euler number	Volume of the biggest air-void	Percolation number	t_2	L_c	Tortuosity
	(%)	(mm)	(mm)		(mm^3)		(min)	(mm)	
1	15.60	1.79	6.42	-132	12656.20	0.96	950	1.70	1.48
2	16.10	1.78	7.04	-142	13813.90	0.94	1060	1.65	1.37
3	17.90	1.72	8.91	-390	14643.60	0.93	1200	1.60	1.34
4	17.80	1.98	7.87	-267	14781.60	0.96	1190	1.50	1.22
5	21.60	2.07	8.29	-332	17834.60	0.99	1700	1.20	1.18
6	22.60	2.43	11.81	-229	18326.70	1.00	1900	1.25	1.13
7	26.30	2.54	9.12	-375	20880.50	1.00	2350	1.00	1.11
8	29.80	2.52	8.07	-340	23218.10	0.99	2500	1.00	1.10

FIGURES

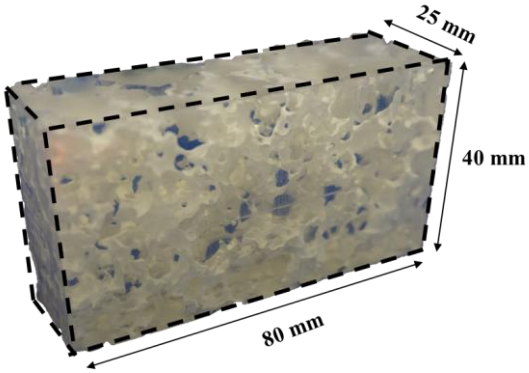

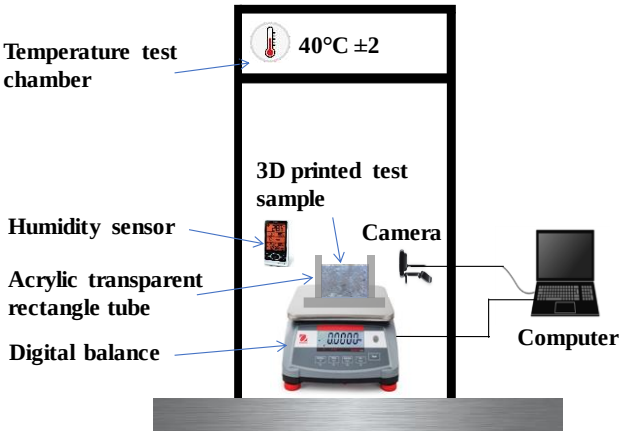

(a) **(b)**

Figure 1:(a) 3D printed transparent resin blocks with equivalent asphalt pore structure with 17.9% porosity (b) Schematic representation of the water evaporation experimental setup.

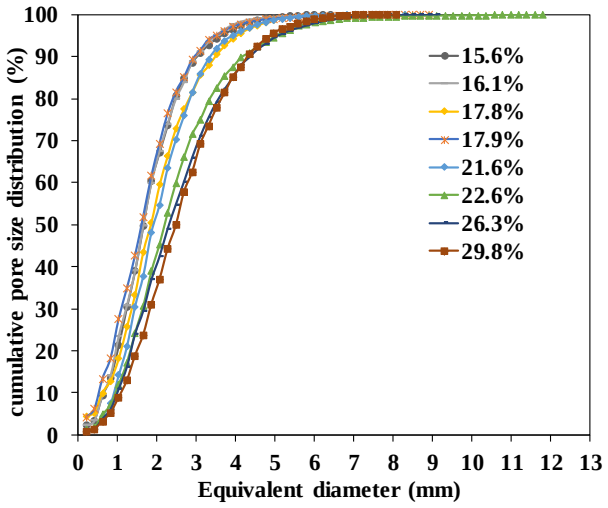

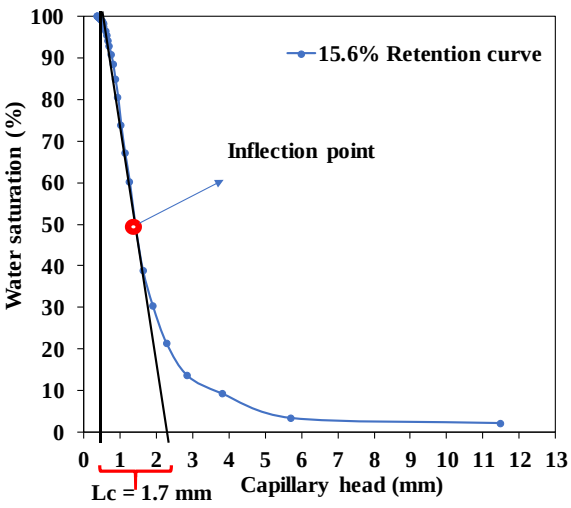

(a) **(b)**

Figure 2: (a) Cumulative pore size distribution of the eight 3D printed samples used in this study and (b) example of water retention curves of asphalt with porosity of 15.6%.

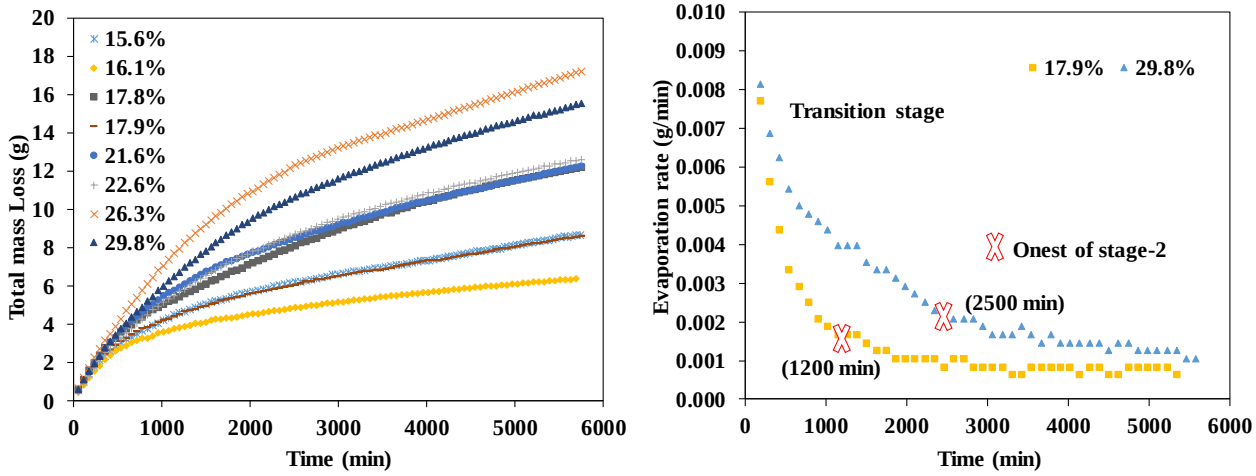

(a) (b)

Figure 3: (a) Total water evaporation loss weight versus time for all samples studied and (b) Water evaporation rate versus time for samples with porosity of 17.9% and 29.8%. The transition period as well as the onset of stage-2 is marked on the figure.

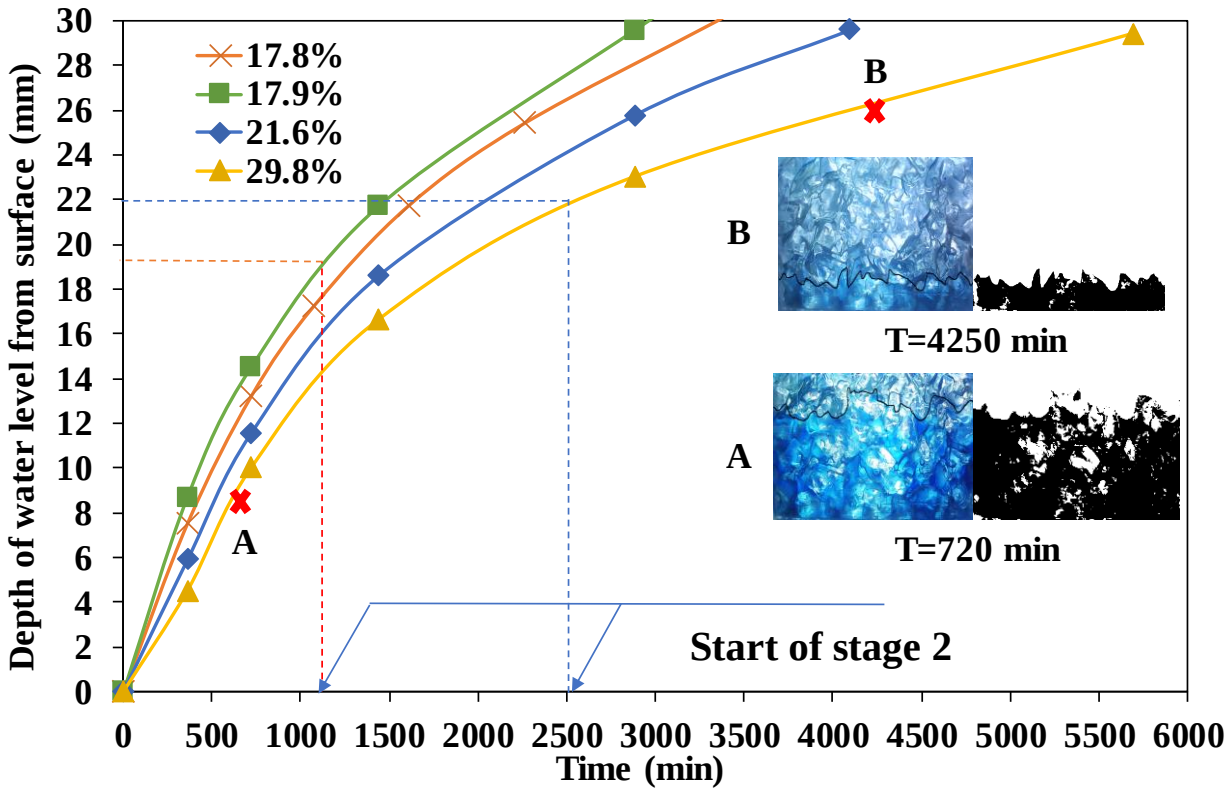

Figure 4: Depth of the evaporation front versus time for 4 test samples with different porosities ranging from 17.8% to 29.8%. Insets show typical examples of the original and segmented images illustrating the morphology of the drying front at two different times from the onset of the experiment with the sample with porosity of 29.8%.

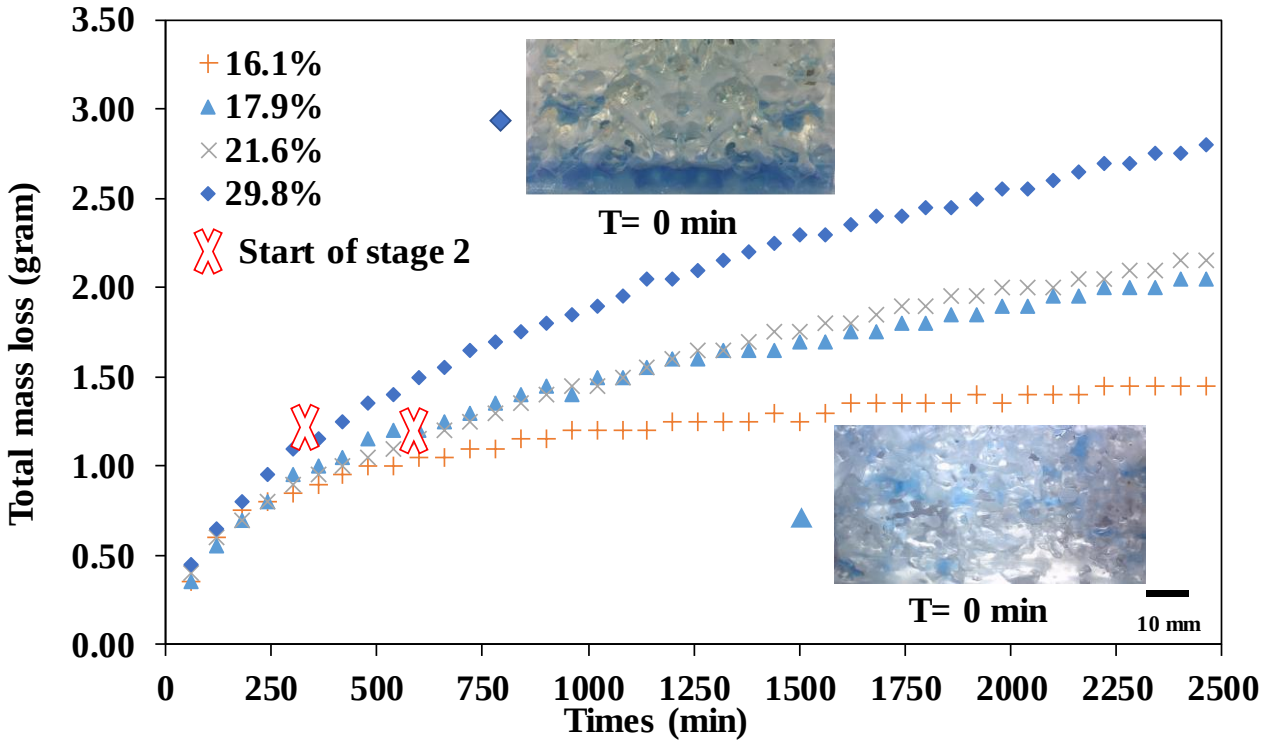

Figure 5: Total water evaporation loss weight versus time measured during evaporation from the semi-saturated samples (the experiments with the drainage). Insets show the water residual distribution just after the end of liquid drainage and before the onset of evaporation experiments for samples with the porosity of 17.9% and 29.8%.

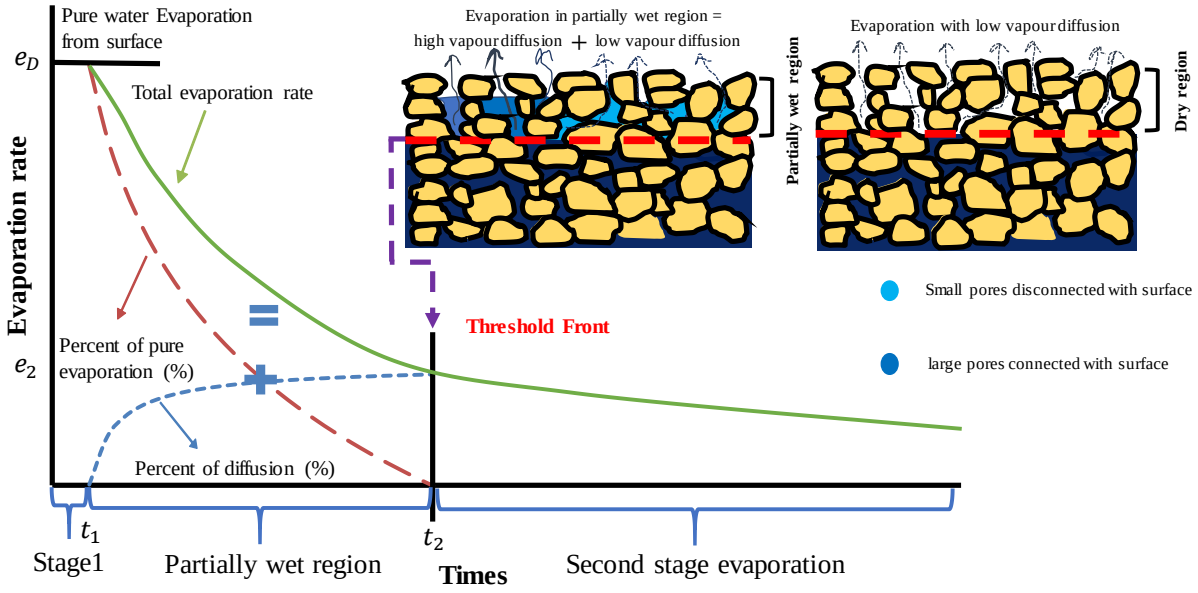

Figure 6: The porposed mechanism to describe the evaporation process from porous asphalt mixture showing the transition and stage-2 evaporation with the conceptual picture presented in the inset.

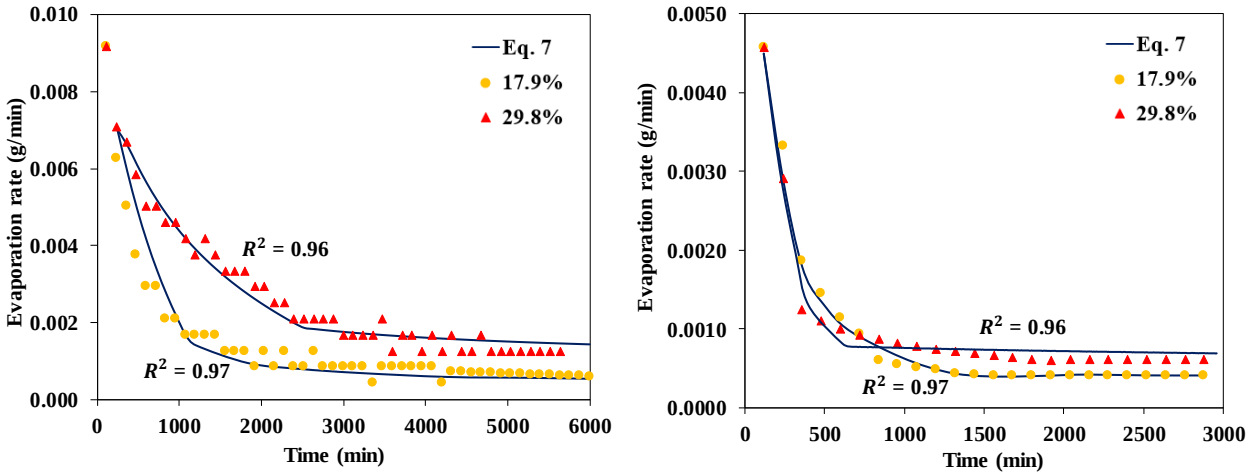

(a) **(b)**

Figure 7: (a) Evaporation rate (g/min) versus time together with the theoretical model corresponding to the test with the saturated case for 3D printed samples with the porosity of 17.9% and 29.8% (b) evaporation rate in semi-saturated case for 3D printed samples with the porosity of 17.9% and 29.8% together with the corresponding theoretical calculations using Eq. 7.